Structural changes, clustering, and photoinduced phase segregation in $Pr_{0.7}Ca_{0.3}MnO_3$

D. E. Cox
Department of Physics, Brookhaven National Laboratory, Upton, New York 11973

P. G. Radaelli
Institut Max Von Laue-Paul Langevin, Boîte Postale 156, 38042 Grenoble Cedex 09, France

M. Marezio
MASPEC-CNR, via Chiavari 18A, 43100 Parma, Italy

S-W. Cheong
Bell Laboratories, Lucent Technologies, Murray Hill, New Jersey 07974
and Department of Physics and Astronomy, Rutgers University, Piscataway, New Jersey 08855
(Received 18 August 1997)

The structural properties of $Pr_{0.7}Ca_{0.3}MnO_3$ were studied by x-ray synchrotron and neutron-powder diffraction as a function of temperature ($15<T<300$ K), and as a function of x-ray fluence at 15 and 20 K. The temperature evolution of the lattice parameters and of the superlattice reflections is consistent with the development of charge and orbital ordering below $T_{CO}\sim 180$ K, followed by antiferromagnetic ordering below $T_N \sim 140$ K, similar to what was previously observed for $La_{0.5}Ca_{0.5}MnO_3$. Below $T_C\sim 120$ K, the magnetic structure develops a ferromagnetic component along the *a* axis on the Mn ions. At low temperatures, a small ferromagnetic moment of $0.45(2)\mu_B$ oriented in the same direction appears on the Pr ions as well. The observation in $Pr_{0.7}Ca_{0.3}MnO_3$ of significant lattice strain developing below T_{CO}, as well as the development of a ferromagnetic component to the magnetic structure at $T_C\sim 120$ K, can be interpreted in terms of the presence of ferromagnetic clusters with an associated lattice distortion from the average structure. At low temperatures, exposure to the x-ray beam produces a phase-segregation phenomenon, whereby the ferromagnetic droplets coalesce into larger aggregates. Further exposure results in a gradual melting of the charge-ordered phase and the formation of a second phase, recently shown to be a ferromagnetic metallic phase by Kiryukhin *et al.* [Nature (London) **386**, 813 (1997)]. The ferromagnetic phase has a significantly smaller *a* lattice parameter and unit-cell volume ($\Delta V/V\sim 0.4\%$) than that of the charge-ordered phase. [S0163-1829(98)00106-4]

I. INTRODUCTION

In the last few years, a significant research effort has been undertaken toward the understanding of the unusual magnetic and transport properties of manganate perovskites. The prototype compound of this family $LaMnO_3$ is an antiferromagnetic insulator characterized by a strong structural distortion interpreted in terms of a cooperative Jahn-Teller (JT) effect, all the manganese ions being in the formal valence state of $+3$.[1,2] Upon partial substitution of La with a divalent alkaline-earth metal, a corresponding fraction x of Mn^{+3} is formally replaced with Mn^{+4}. For compositions $0.2\leqslant x \leqslant 0.4$ the compounds are ferromagnetic and exhibit colossal magnetoresistance (CMR).[3,4] The doped systems, with general formula $A_{1-x}A'_xMnO_3$ (A=La, rare earth, A'=Ca, Sr, Ba), are characterized by a strong competition between two different ground states: a charge-ordered (CO) insulating state, where the electric charges are localized and tend to order onto separate crystallographic sublattices, and a charge-delocalized (CD) state, having metallicklike dc conductivity.[5–7] The magnetic and structural properties of these two states are also quite different: the CO state is antiferromagnetic (AFM), and the Mn^{+3} sublattice retains a cooperative JT distortion, thereby giving rise to an often complex combination of charge, orbital, and magnetic ordering.[1,2,8–10] On the other hand, the CD state is ferromagnetic (FM), and displays relatively small JT distortions.[11–14] The ferromagnetic properties of these compounds have been explained in the context of the so-called double-exchange model, originally proposed by Zener in 1951,[15] and further developed by Anderson and Hasegawa[16] and by de Gennes.[17] When heated above a characteristic temperature, both the CO and the CD states transform to a ''charge-localized'' (CL) paramagnetic phase, characterized by low electronic carrier mobility, semiconducting behavior of the electrical resistivity, and significant lattice distortions, which are mainly of the incoherent type.[11–14,18] The CD-CL transition is characterized by a significant increase in the electrical resistivity upon heating, and is rather sensitive to the application of an external magnetic field, giving rise to the so-called colossal magnetoresistance effect.[4]

The nature of the CL paramagnetic phase has been one of the main focuses of the experimental and theoretical work in this field. In particular, some calculations have suggested that the value of the electrical resistivity in this phase is too high to be explained by spin scattering alone,[19–24] and consequently alternative charge localization mechanisms have been sought. Millis and co-workers have proposed that, in

the CL phase, charge carriers may be localized by lattice distortions of the JT type,[21,23,24] the existence of which has been confirmed by several techniques, including diffraction,[11,13,14,18,25] neutron-diffraction pair-distribution-function (PDF) analysis,[12] extended x-ray-absorption fine structure (EXAFS),[26,27] optical conductivity,[28,29] infrared reflectivity,[30] muon spin relaxation,[31] photoemission,[32] and oxygen isotope effect.[33,34] More recently, Lynn *et al.*[35] and De Teresa *et al.*[36] have demonstrated the existence in the CL phase of ferromagnetic clusters well beyond the conventional fluctuation regime, and interpreted them in terms of magnetic polarons. This theoretical and experimental work has not yet led to a unified model of the CL phase. However, the JT polaron model and the magnetic polaron model could be reconciled under the assumption that the JT polarons (associated with fluctuating JT distorted regions of the lattice) break the long-range ferromagnetic (FM) coherence, leaving relatively small (10–20 Å) FM clusters where the lattice is relatively undistorted. We shall see in the remainder of this paper how this model can help to explain the unusual properties of $Pr_{0.7}Ca_{0.3}MnO_3$.

The energetic balance between the CO, CD, and CL phases can be altered not only by changing the electronic doping, but also by other physical and chemical means; for example, the CD phase is stabilized by the application of an external magnetic field or pressure, whereas the CO or CL phases are stabilized by an increase in the structural distortion from the ideal cubic perovskite-type lattice. The latter effect can be obtained by replacing La with smaller rare-earth ions, such as Pr, Y, and Tb, thereby reducing the average A-site ionic radius $\langle r_A \rangle$. For instance, it has been shown that for $x=0.3$, a low-temperature metal-insulator (M-I) transition occurs as a function of $\langle r_A \rangle$ at a critical radius $r_{M-I} \sim$ 1.2 Å.[7] The region of the phase diagram near the low-temperature M-I transition is particularly interesting, since the strong competition between CO and CD phases gives rise to a number of unique features, and the electrical resistivity changes by several orders of magnitude as a function of applied magnetic field or applied pressure.[9,37,38] In this region of the phase diagram, the composition $Pr_{0.7}Ca_{0.3}MnO_3$ is an ideal test system, due to the almost perfect matching of the A-site ionic radii, and has been the subject of several studies. The first comprehensive structural study of the $Pr_{1-x}Ca_xMnO_3$ system was carried out by conventional x-ray-powder-diffraction techniques by Pollert *et al.*,[39] who noted the disappearance of the strong cooperative JT distortion for $x \geqslant 0.3$ and proposed the formation of local JT distortions. A subsequent neutron-powder-diffraction study by Jirák *et al.*[8] revealed a CO transition in the region 200–250 K, followed by AFM and FM transitions at ~ 130 and 110 K, respectively. Jirák *et al.* interpreted this as the coexistence of two phases in about equal amounts rather than a transition from an AFM to a canted structure. They also noted that the 200 K transition was characterized by the appearance of weak superlattice reflections which could be indexed on the basis of a doubled orthorhombic cell ($a,2b,c$-$Pbnm$ setting or $2a,b,c$-$Pnma$ setting[40]). Their proposed structure shows shifts of the Mn atoms qualitatively similar to those found in $La_{0.5}Ca_{0.5}MnO_3$,[10] although they assigned a different symmetry to this superstructure ($Pbmm$ vs $P2_1/m$).

A detailed neutron single crystal of $Pr_{0.7}Ca_{0.3}MnO_3$ study by Yoshizawa *et al.*[9] confirmed the CO transition at about 200 K from the appearance of the (3/2 0 2) reflection, and the AFM and FM transitions at 140 and 110 K, respectively, from the behavior of the (1/2 1/2 0) and (110) reflections. They interpreted these results in terms of a canted AF structure, but because of the rather small total moment of $\sim 2.4\mu_B$, they suggested that some fraction of the moments formed a spin-glass state due to the presence of excess Mn^{+3} ions. Application of a magnetic field at 5 K resulted in an enhancement of the FM (110) peak and a large decrease in the AF (1/2 1/2 0) and CO (1/2 0 2) peaks, consistent with a field-induced CO-CD transition; however, the intensity of the CO peak did not vanish completely. At 5 K the FM state was retained when the field was released. In a neutron-powder-diffraction study of $Pr_{0.6}Ca_{0.4}MnO_3$ Lees *et al.*[41] obtained rather similar results, namely, a CO transition at 250 K, an AFM transition at 160 K, and a field-induced AFM-FM transition at ~5 T. Tomioka *et al.*[42] mapped out the H-T phase diagram in detail for single crystal samples with $0.3 \leqslant x \leqslant 0.5$ and showed that for $Pr_{0.7}Ca_{0.3}MnO_3$ the CO state could not be restored until the temperature was increased above $T_{irr} \sim 60$ K, the low-temperature FM state being considered as metastable. From thermal expansion and magnetostriction measurements on a polycrystalline sample with $x=0.33$, De Teresa *et al.*[43] noted a crossover from a CL to a CO state in the 200 K region above $T_{CO} \sim 210$ K, and a first-order field-induced transition from the CO to a CD state accompanied by a volume decrease of ~0.14%. In a recent neutron single crystal experiment, Yoshizawa *et al.*[44] observed a pressure-induced I-M transition for $Pr_{0.7}Ca_{0.3}MnO_3$ at 0.7 and 2 GPa. In the latter case, no CO or AFM peaks were seen above $T_C \sim 150$ K.

A recent paper by Kiryukhin *et al.*[45] reports an x-ray photoinduced I-FM transition at 4 K in a $Pr_{0.7}Ca_{0.3}MnO_3$ single crystal, characterized by a rapid decrease in the intensity of the CO (3/2 0 2) peak as a function of exposure time in a synchrotron x-ray beam (energy 8 keV, flux $\sim 5 \times 10^{10}$ photons/mm^2/s), together with a large decrease in resistivity. These effects were not reversible at 4 K, but the induced conductivity could be annealed out above 60 K. The CO (3/2 0 4) peak was also monitored with neutrons, but did not show any unusual behavior.

In this paper, we present synchrotron x-ray and neutron-powder-diffraction data for $Pr_{0.7}Ca_{0.3}MnO_3$ powder samples as a function of temperature, and x-ray-diffraction data as a function of x-ray exposure time. Our data clearly show that the photoinduced CO-CD low-temperature phase transition is associated with phase segregation. The as-cooled sample is single phase, but the Bragg peaks display a significant anisotropic strain. The presence in the powder patterns of superlattice peaks, which can be indexed on a unit cell with the a axis doubled, provides clear evidence of charge ordering. Soon after opening the x-ray shutter, this anisotropic strain leads to the development of two well-defined crystallographic phases with different unit cell volumes. Upon further exposure to x-rays, the proportion of the two phases gradually changes, and the intensity of the superlattice peaks decreases with a similar time constant. The proportion of the phase having the smaller unit cell volume increases as a function of time, strongly suggesting that the latter is the

ferromagnetic metallic CD phase. In the light of these results, the very large values of the magnetoresistance in this and similar compounds can be explained assuming that the field-induced transition has a similar two-phase nature. In fact, in this case, the electrical resistivity would drop abruptly as soon as the CD phase attains the percolation threshold. We believe that the presence of significant anisotropic strain in the as-cooled samples is also an extremely important feature. This strain, which gradually develops below the charge-ordering temperature $T_{CO} \sim 180$ K, indicates the presence of structural inhomogeneities, which may provide an alternative explanation for the simultaneous presence of ferromagnetic and antiferromagnetic magnetic peaks in this compound. In this scenario, the ferromagnetic peaks would be associated with frozen-in clusters characterized by a smaller-than-average unit-cell volume, rather than with a uniform canting of the antiferromagnetic structure.

II. X-RAY AND NEUTRON DIFFRACTION

The polycrystalline sample of $Pr_{0.7}Ca_{0.3}MnO_3$ was prepared by conventional solid-state techniques and was part of the same batch of material described in Ref. 7. Synchrotron x-ray-powder-diffraction data were collected at the X7A beamline at the National Synchrotron Light Source at Brookhaven National Laboratory, from a flat-plate sample mounted in symmetric reflection geometry in a closed-cycle He cryostat. The instrument configuration consisted of a double-crystal Ge(111) monochromator and a flat Ge(220) analyzer crystal in the diffracted beam set for a wavelength of 1.2003 Å. The intrinsic resolution with this configuration is about 0.01° in the low-angle 2θ range between 10–40°. Step scans were made over selected low-angle reflections at a number of temperatures between 15–325 K during both cooling and heating cycles, and extended data sets were collected at 300, 160, 80, and 15 K. The step interval was 0.005°, and the sample was rocked through a few degrees at each point to ensure proper powder randomization. Because of the gradual evolution of a second phase during data collection at 15 K, believed to result from the photoinduced transition recently reported by Kiryukhin *et al.*,[45] subsequent measurements were made on the same sample after cooling from 300 to 20 K. Two data sets were obtained as a function of x-ray fluence: the first immediately after cooling the sample to 15 K, the second after equilibrating it at 20 K for 44 h before exposure to the x-ray beam. For the latter measurements, a Si(111) monochromator was used at a wavelength of 1.1997 Å, and the evolution of the second phase at 20 K was followed by repeated scans of the (220)/(022) pair of reflections[40] as a function of time. The lattice parameters at each temperature were determined from a least-squares fit to the positions of several low-angle peaks obtained from fits to a pseudo-Voigt peak shape function.[46] The latter process was complicated by the fact that some of the closely adjacent peaks, such as the (202)/(040) pair derived from splitting of the pseudocubic (200) reflection, were observed to have markedly different widths and shapes (see Sec. V), necessitating the use of individual full widths at half maximum (FWHM's) and mixing parameters as well as peak positions and integrated intensities in the fits.

In order to determine the evolution of the magnetic structure, medium-resolution neutron-powder-diffraction data were collected as a function of temperature on the D1B diffractometer at the Institut Laue-Langevin (ILL), using a wavelength of 2.520 Å. High-resolution neutron-powder-diffraction data were collected at 1.5 K on the D2B diffractometer at the ILL. In order to optimize both resolution and reciprocal space range, data sets were collected at two different wavelengths and instrument configurations: $\lambda_1 = 1.594$ Å in the high-intensity mode, with no primary beam collimation, a monochromator mosaic spread FWHM of $\sim 15'$, and $5'$ collimation between sample and detector, and $\lambda_2 = 2.400$ Å in the high-resolution mode, using a 3-cm thick highly oriented pyrolytic graphite filter in the primary beam to eliminate $\lambda/2$ and $\lambda/3$ contamination (less than 0.1 and 0.2 %, respectively). For these measurements, the monochromatic beam divergence α_2 was limited to $\sim 0.2°$ by means of a slit system positioned ~ 15 cm after the monochromator, but otherwise the same configuration was used for the primary beam and detector collimation as for the 1.594 Å data collection. This allowed a resolution of $\Delta 2\theta$ of $\sim 0.2°$ to be attained up to $2\theta \leqslant 100°$. The complete x-ray and neutron patterns were analyzed by the Rietveld method[47] using the GSAS (Ref. 48) and FULLPROF (Ref. 49) programs.

III. MAGNETIC STRUCTURE

The $Pr_{0.7}Ca_{0.3}MnO_3$ thermodiffractogram, obtained from the D1B neutron-powder-diffraction data by subtracting the 150 K data set from the data sets collected at lower temperatures, reveals the appearance, on cooling, of two sets of Bragg peaks at $T_N \sim 140$ K and $T_C \sim 120$ K, respectively. The 120 K peaks have the propagation vector [0,0,0] (G point of the first Brillouin zone), and are consistent with FM coupling of the moments on the Mn sublattice. The 140 K peaks can be indexed using the two propagation vectors [1/2,0,1/2] (U point of the first Brillouin zone) and [0,0,1/2] or [1/2,0,0] (Z or X point of the first Brillouin zone), which are associated with the previously described AFM ''pseudo-CE'' or ''CE-type'' magnetic structures.[8] Unlike the case of $La_{0.5}Ca_{0.5}MnO_3$, both sets of magnetic peaks are resolution limited even for the high-resolution D2B data set collected at 2.400 Å. A close inspection of the D1B data reveals the presence of a third rather subtle magnetic transition in the region 40–60 K, which manifests itself as an increase in the ratio between the simple perovskite (110) and (100) magnetic Bragg peaks, which are split into (200,002,121) and (101,020) sets, respectively, in the orthorhombic cell using the $Pnma$ setting. This effect can be attributed to the development of a ferromagnetic moment on the Pr ions, located on the perovskite A site, parallel to the FM-coupled Mn moments. The magnetic and crystal structures were simultaneously refined at 1.5 K using the two D2B data sets. The intensity ratios between the AF peaks clearly indicate that the moments are oriented along the b axis, as previously reported.[42] The AFM moments on the two sublattices were refined independently, but turned out to be almost identical within the error bars. As far as the FM moments are concerned, the best fits were obtained with the moments aligned along the a axis. A significant improvement of the agreement factors was obtained with a refined FM moment of $0.45(2)\mu_B$ on the Pr site, oriented in the same direction as the

TABLE I. Refined magnetic moment for the $Pr_{0.7}Ca_{0.3}MnO_3$ magnetic structure at 1.5 K (D2B) data at $\lambda_1 = 1.594$ Å and $\lambda_2 = 2.400$ Å. The magnetic moments are expressed in Bohr magneton, and the site coordinates are expressed as fractions of the $2a \times b \times c$ magnetic cell.

Mn AFM [1/2,0,0] propagation vector		Mn AFM [1/2,0,1/2] propagation vector	
sites	μ_y	sites	μ_y
0 1/4 0	1.48(2)	1/4 1/4 1/4	1.53(2)
1/2 1/4 0		3/4 1/4 3/4	
0 3/4 1/2		1/4 3/4 3/4	
1/2 3/4 1/2		3/4 1/4 1/4	
0 1/4 1/2	−1.48(2)	1/4 1/4 3/4	−1.53(2)
1/2 1/4 1/2		3/4 1/4 1/4	
0 3/4 0		1/4 3/4 1/4	
1/2 3/4 0		3/4 3/4 3/4	
Mn-FM $\mu_x = 2.20(2)$		Pr-FM $\mu_x = 0.45(2)$	

Mn FM moment. The crystallographic structural parameters refined from the D2B data are published elsewhere,[50] and the magnetic parameters are reported in Table I. The temperature-dependent magnetic moments (Fig. 1) were obtained from sequential Rietveld refinement based on the D1B data, with the structural parameters fixed at the low-temperature values determined using D2B data. The small value of the Pr moment did not permit a precise location of the *A*-site FM ordering transition, and the FM Pr moment was accordingly refined only below 60 K.

In the case of $La_{0.5}Ca_{0.5}MnO_3$, early work demonstrated a close link between the magnetic ordering on the one hand and the charge and orbital ordering on the other. Already in 1955, Goodenough[2] proposed that the CE-type magnetic

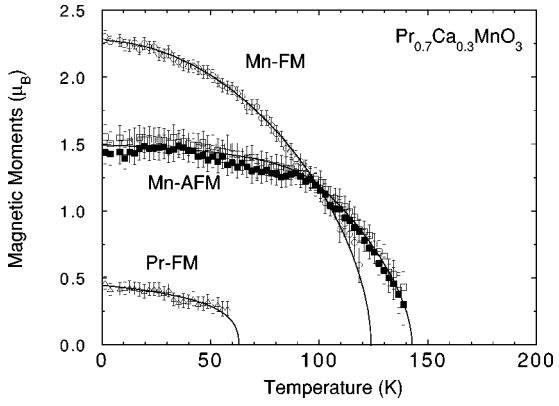

FIG. 1. Magnetic moments as a function of temperature for $Pr_{0.7}Ca_{0.3}MnO_3$, obtained from a sequential Rietveld refinement of the D1B temperature-dependent neutron powder diffraction data ($\lambda = 2.520$ Å). The symbols are Mn-FM moment (open circles); Mn-AFM moments with propagation vector [1/2,0,1/2] (open squares); Mn-AFM moments with propagation vector [1/2,0,0] (filled squares); Pr-FM moments (open triangles). Solid lines are guides to the eye. The structural parameters were kept fixed at the low-temperature values determined from the D2B data.

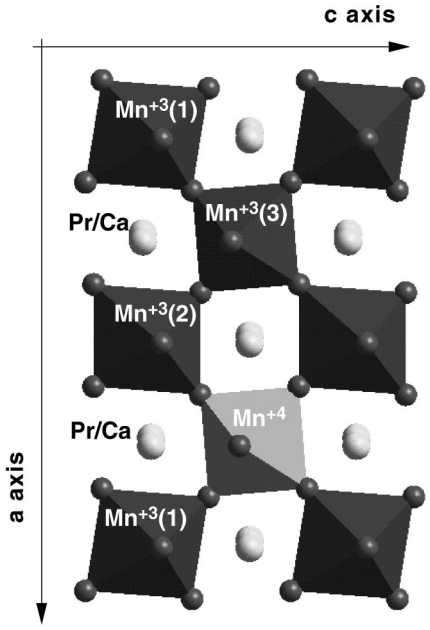

FIG. 2. Schematic representation of the $Pr_{0.7}Ca_{0.3}MnO_3$ charge- and orbitally-ordered superstructure, assumed to have space group symmetry $P2_1/m$ (Ref. 10). Mn^{+3} and Mn^{+4} are shown as dark and light octahedra, respectively. The Mn(1) and Mn(2) sites, which have twofold multiplicity, are occupied only by Mn^{+3}. The d_{z^2} orbitals on this site are ordered in the *a*-*c* plane as in $La_{0.5}Ca_{0.5}MnO_3$. The Mn(3) site (central column), which has fourfold multiplicity, is randomly occupied by Mn^{+4} (60%) and Mn^{+3} (40%), the latter having d_{z^2} orbitals oriented along the *b* axis.

structure could be constructed from the charge-ordered structure by assuming that the Mn-O-Mn superexchange interaction is ferromagnetic when one of the Mn-O bonds is ''long'' due to the JT distortion (involving a filled $Mn^{+3}d_{z^2}$ orbital), and antiferromagnetic when both Mn-O bonds are short. The recently determined charge-ordered and orbitally ordered superstructure of $La_{0.5}Ca_{0.5}MnO_3$ (Ref. 10) has fully confirmed this hypothesis. It is interesting to apply to $Pr_{0.7}Ca_{0.3}MnO_3$ the same qualitative considerations that led to the hypothesis of charge and orbital ordering in $La_{0.5}Ca_{0.5}MnO_3$ on the basis of its magnetic structure. The antiferromagnetic component of the $Pr_{0.7}Ca_{0.3}MnO_3$ magnetic structure, known as the ''pseudo-CE'' structure, is closely related to the CE-type structure, the magnetic coupling in the *a*-*c* plane being identical in each case, with FM-coupled zig-zag AFM chains running along the *a* or *c* axes. Apart from the orientation of the magnetic moments the main difference between the two structures is the way the layers are coupled along the *b* direction: the coupling is AFM in the CE structure and FM in the pseudo-CE structure. Based on the Goodenough model,[2] one would conclude that the orbital ordering is the same for the two structures in the *a*-*c* plane, but that the pseudo-CE structure accommodates a significant number of long Mn-O bonds directed along the *b* axis, yielding a net FM interlayer coupling. The following simplified model, shown schematically in Fig. 2, may therefore be proposed for the $Pr_{0.7}Ca_{0.3}MnO_3$ superstructure. (1) As in the case of $La_{0.5}Ca_{0.5}MnO_3$ the superstructure would be made up of three sublattices Mn(1), Mn(2), and Mn(3), with all the $Mn^{+3}O_6$ octahedra assumed to be JT distorted

(4 short and 2 long Mn^{+3}-O bonds). (2) The Mn(1) and Mn(2) sublattices would contain only Mn^{+3} as in the case of $La_{0.5}Ca_{0.5}MnO_3$, and would have the same orbital ordering, with all the long Mn^{+3}-O bonds oriented in the a-c plane. (3) The Mn(3) sublattice, which for $La_{0.5}Ca_{0.5}MnO_3$ was occupied by Mn^{+4} alone, would now contain 40% of Mn^{+3} and 60% of Mn^{+4}, all the long Mn^{+3} -O bonds being directed along the b axis. As we shall see in Secs. IV and V, the intensities of the superlattice reflections and the temperature dependence of the lattice parameters are in qualitative agreement with this model, once the effects of structural disorder are taken into account. We should remark, however, that for this model only the Mn ions on the Mn(3) sites give rise to FM coupling along the b axis, since the coupling for the Mn(1) and Mn(2) sites along the b axis continues to be AFM. For this kind of highly frustrated system, the observed magnetic structure is therefore explicable only if it is assumed that an overall FM coupling results from the competition between FM and AFM b-axis coupling. Furthermore, significant structural disorder could be introduced because of the tendency of the Mn^{+3}(1)-O-Mn^{+3}(1) and Mn^{+3}(2)-O-Mn^{+3}(2) linkages (two empty $d_{x^2-y^2}$ orbitals) to be shorter than the Mn^{+3}(3)-O-Mn^{+4} linkage (one filled d_{z^2} and one empty $d_{x^2-y^2}$ orbital).

The neutron-diffraction data reveal an increase in the intensity at the nuclear peak positions below $T_C \sim 120$ K, consistent with the development of a ferromagnetic moment. This FM component has previously been described either in terms of two coexisting phases[8] or a noncollinear canted structure.[18,42] It is important to point out that, although the spin orientation as determined from previous studies and the present one is not incompatible with spin canting, it is extremely difficult to discriminate between the two phase and the canting models in the absence of accurate polarized neutron studies. However, it is clear from the present diffraction data that no long-range phase segregation, either spontaneous or photoinduced, takes place between T_C and $T_{\rm irr}$, indicating that a simple two-phase model is not valid. Also, the larger value of the FM moment compared to the average AFM moment, 2.20(2) vs $1.50(2)\mu_B$, allows one to conclude that it can arise only from the double-exchange interaction, and not from other possible mechanisms, such as next-nearest-neighbor interactions.

The canting model, which results from the competition between ferromagnetic double-exchange and antiferromagnetic superexchange, has been extensively discussed in a classic paper by de Gennes.[17] However, as de Gennes points out, uniform canting can be achieved only in the presence of free carriers, i.e., in a metal, whereas the present system is an insulator. Bound carriers would give rise to a local ferromagnetic distortion of the spin system, which would therefore become inhomogeneous.[17] In the latter case, the bound Zener electrons would form small ferromagnetic clusters in an otherwise antiferromagnetic matrix, and the cluster spins would then align parallel to each other at T_C. The presence of ferromagnetic clusters in perovskite manganates above the spin ordering temperature is now well documented.[35,36] Also, there is evidence that these clusters may be associated with a local lattice ''distortion''[36] (the term is rather misleading, since the FM regions are expected to be relatively undistorted with respect to the JT distorted polaronic regions in the matrix). Therefore, the observation of increased lattice strain below $T_{\rm CO}$ (see Sec. V) constitutes an indirect confirmation of the inhomogeneous model.

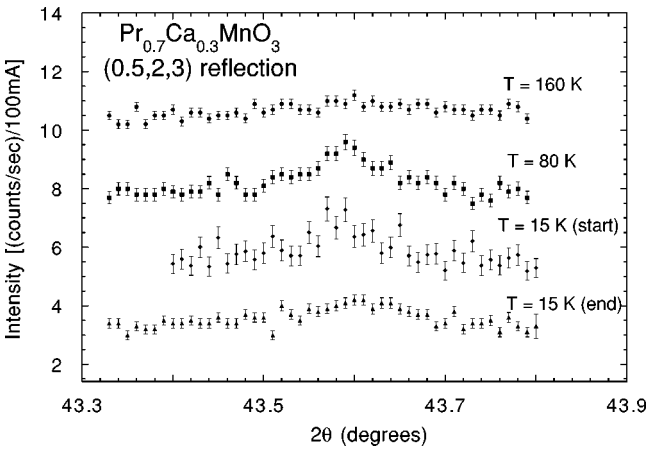

FIG. 3. Portions of the synchrotron x-ray-powder-diffraction patterns for $Pr_{0.7}Ca_{0.3}MnO_3$ at 160, 80, and 15 K, in the region of the (1/2 2 3) superlattice peak. The two data sets at 15 K were obtained immediately after cooling down (start) and after ~17 h exposure to the x-ray beam, corresponding to a fluence of 8.5×10^{13} photons/mm^2 (end).

IV. SUPERLATTICE PEAKS

Previous neutron-diffraction measurements by Jirák *et al.*[8] and Yoshizawa *et al.*[9] showed that the CO structure is characterized by doubling of the a axis and the appearance of additional peaks of the type $(h/2\ k\ l)$. The presence of these superlattice reflections is evident in both the x-ray and neutron-diffraction data. In the latter, however, the intensity resulting from the nuclear superstructure [associated, for instance, with the (1/2 0 2) and (3/2 0 2)/(1/2 2 2) peaks] is always accompanied below T_N by a magnetic contribution due to the AFM structure. For this reason, we have used the x-ray data to characterize the superstructure. A careful search was made for superlattice peaks associated with charge ordering of Mn^{+3} and Mn^{+4} below $T_{\rm CO} \sim 200$ K. Because the superlattice peaks were expected to be very weak, the search was limited to narrow regions covering the strongest of these peaks observed in our previous measurements on $La_{0.5}Ca_{0.5}MnO_3$.[10] The initial measurements were carried out at 80 K where the superlattice intensity is approaching saturation[9] and well above the temperature range where the photoinduced ''charge-melting'' transition occurs.[45] With very long counting times of 120 sec per step, definite evidence of charge ordering was seen at positions corresponding to the (3/2 0 2)/(1/2 2 2) pair and the (1/2 2 3) peak, which are the strongest of the superlattice reflections observed for $La_{0.5}Ca_{0.5}MnO_3$.[10] Furthermore, in contrast to the findings for the latter compound, the modulation vector was commensurate within an experimental error of 0.003. The intensity data for the (1/2 2 3) peak, which is well resolved from adjacent fundamental peaks, are displayed in Fig. 3, together with the results of similar scans at 160 and 15 K. In the latter case, the elapsed times at the midpoint of the scan were ~30 and ~1020 min, respectively, for the scans labeled ''start'' and ''end'' (see Sec. VI). Because of the long counting times

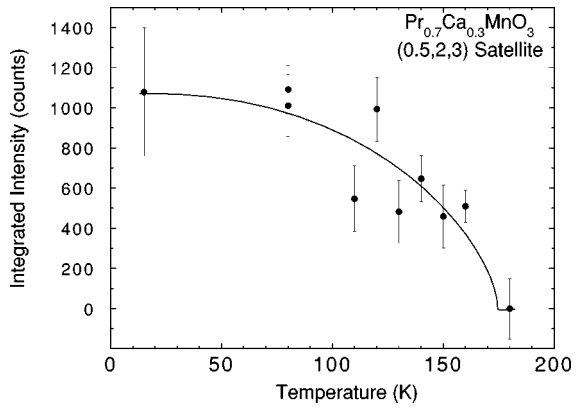

FIG. 4. Intensity of the (1/2 2 3) peak as a function of decreasing temperature for $Pr_{0.7}Ca_{0.3}MnO_3$. The data point at 15 K was obtained immediately after cooling. The solid line is a guide to the eye.

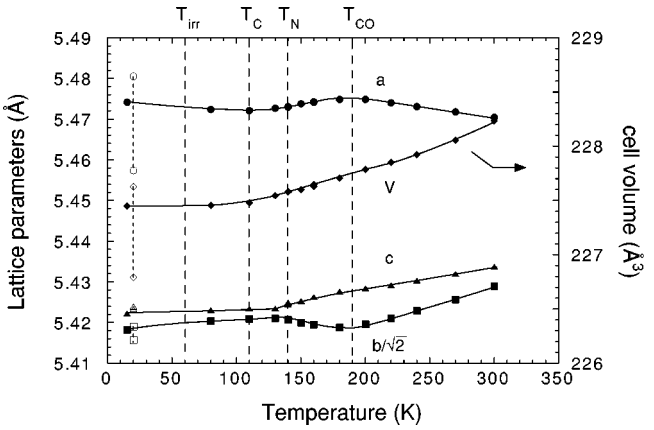

FIG. 5. Lattice parameters and unit cell volume as a function of temperature for $Pr_{0.7}Ca_{0.3}MnO_3$ determined from synchrotron x-ray powder diffraction data. The filled symbols at 15 K indicate the values for the single phase obtained immediately after cooling. The empty symbols connected by vertical dotted lines represent the values at 20 K for the two coexisting phases obtained after ~31 h exposure to the x-ray beam, corresponding to a fluence of 15.9×10^{13} photons/mm^2. The solid lines are guides to the eye.

needed for complete scans of the CO peaks, it was not feasible in the time available to make detailed measurements of their temperature dependence. However, an approximate determination of the (1/2 2 3) intensity was made at several temperatures from measurements at the peak position and a background point at each side. These values, scaled by the ratio of the integrated and peak values at 80 K, are plotted in Fig. 4, from which it can be seen that T_{CO} lies in the region of 180–200 K (for the 15 K point, the data recorded immediately after cooling down were used as described in Sec. VI). The observed intensities in five regions are qualitatively accounted for by a structural model similar to that previously proposed,[10] in which the MnO_6 octahedra around the Mn^{+4} sites are shifted along c towards two neighboring Mn^{+3} atoms by ~0.05 Å, and two of the surrounding Pr/Ca atoms are shifted in the same direction by ~0.03 Å (Table II). It should be noted that these shifts are only about one half of those observed for $La_{0.5}Ca_{0.5}MnO_3$, and that the intensities of the CO peaks are $\lesssim$0.1% of those of the strongest fundamental peak (a factor of 3–4 lower than in the case of $La_{0.5}Ca_{0.5}MnO_3$). Although it is possible to interpret this discrepancy in terms of a uniformly reduced JT distortion of the $Mn^{+3}O_6$ octahedra, it is very likely that the reductions in the superlattice peak intensity actually arise from structural disorder. As we shall see in Sec. V, the observation of significant stain broadening in the diffraction data strongly suggests the existence of regions of the lattice where the local structure differs significantly from the average one.

TABLE II. Comparison of observed and calculated intensities for the charge-ordered structure of $Pr_{0.7}Ca_{0.3}MnO_3$ at 80 K, based on the monoclinic structure with doubled a axis proposed for $La_{0.5}Ca_{0.5}MnO_3$ in Ref. 10, with $\Delta z = 0.1$ and $\Delta z' = 0.05$. Estimated errors for I(obs) are given in parentheses. Values of I(calc) were scaled based on a Rietveld fit to the average structure with *Pnma* symmetry.

hkl	I(obs)	I(calc)
$121,12\bar{1}$	4(5)	7
$102,10\bar{2}$	4(5)	8
$302,30\bar{2}$		
$122,12\bar{2}$	25(5)	21
$123,12\bar{3}$	15(5)	15
$323,32\bar{3}$	16(10)	14

V. STRUCTURAL PARAMETERS AS A FUNCTION OF TEMPERATURE

The temperature dependence of the lattice parameters, as determined from the synchrotron x-ray-powder-diffraction data, is shown in Fig. 5. Their behavior, which is in qualitative agreement with previously published data on similar compounds,[18] is rather complex. Near room temperature, the evolution of the lattice parameters is typical for orthorhombic perovskites, i.e., the b axis and the unit-cell volume decrease while the orthorhombic strain increases with decreasing temperature. However, the low-temperature behavior is characterized by the presence of a number of changes in slope corresponding to the characteristic structural and magnetic ordering temperatures T_{CO}, T_N, and T_C. In contrast to $La_{0.5}Ca_{0.5}MnO_3$, which also undergoes charge ordering (T_{CO}~230 K), the $Pr_{0.7}Ca_{0.3}MnO_3$ lattice parameters behave in a strikingly different fashion. In particular, for $La_{0.5}Ca_{0.5}MnO_3$ the b axis rapidly drops in the vicinity of T_{CO}, while the a and c axes increase, consistent with the absence of a volume anomaly. In contrast, for $Pr_{0.7}Ca_{0.3}MnO_3$ the behavior is opposite in sign, namely, the b axis increases at T_{CO}, and the change is much smaller in absolute value. This observation can be explained within the framework of the proposed model for the $Pr_{0.7}Ca_{0.3}MnO_3$ superstructure. The increase in the b axis at T_{CO} suggests that the decrease expected because of orbital ordering of Mn^{+3}in the a-c plane is more than compensated for by alignment of the d_{z^2} orbitals of the excess Mn^{+3} along the b axis, resulting in roughly the same fraction of such orbitals in both the disordered (above T_{CO}) and CO phases. The a parameter exhibits opposite behavior, while c decreases fairly

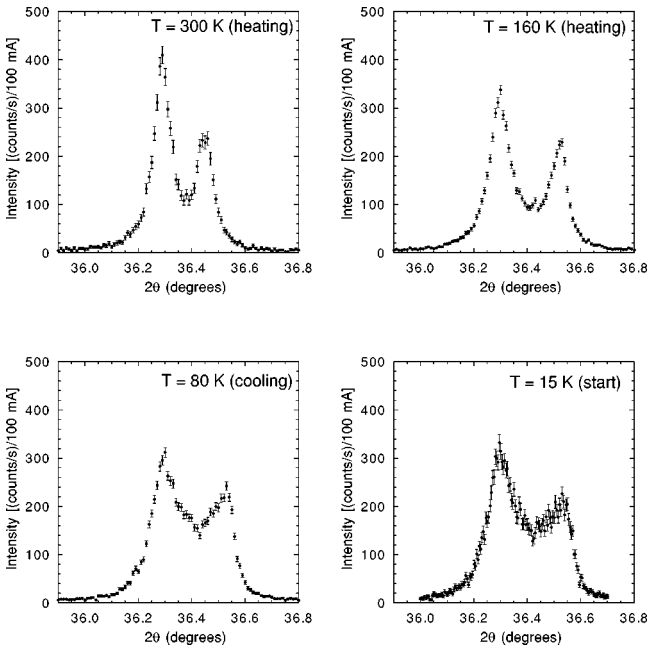

FIG. 6. Anisotropic strain broadening below T_{CO} for $Pr_{0.7}Ca_{0.3}MnO_3$ showing the evolution of the (202)/(040) doublet as a function of decreasing temperature.

steadily with decreasing temperature, showing only a relatively weak inflection point in the vicinity of T_{CO}. In common with $La_{0.5}Ca_{0.5}MnO_3$, there is little evidence of any anomalies in the cell volume, and the orbital ordering process, as evidenced by the lattice constant anomalies, is essentially complete at T_N. Between T_N and T_{irr} the lattice parameters resume the trend seen above T_{CO}, with a notable absence of any anomalies at T_C. Below T_{irr}, the values of the lattice parameters and the unit-cell volume, as determined from the synchrotron data, are strongly dependent on sample history, due to the photoinduced phase segregation phenomenon described in Sec. VI.

As in the case of $La_{0.5}Ca_{0.5}MnO_3$, the temperature region between T_{CO} and T_N is associated with the development of significant and selective broadening of the Bragg peaks. This behavior is illustrated in Figs. 6 and 7, and is accompanied by a buildup of additional scattering between the peaks. In

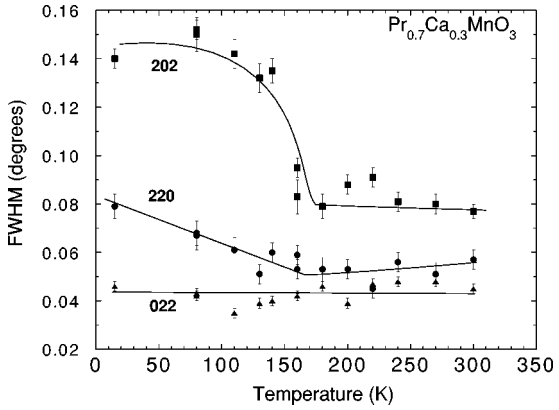

FIG. 7. FWHM's as a function of temperature for the (202), (220), and (022) synchrotron x-ray peaks. The solid lines are guides to the eye.

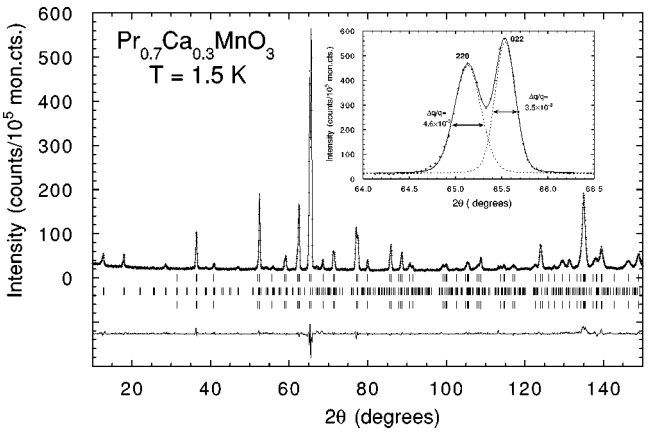

FIG. 8. Rietveld refinement pattern and difference plot of the high-resolution neutron-powder-diffraction data ($\lambda = 2.400$ Å), refined with FULLPROF (Ref. 49) using an orthorhombic anisotropic strain broadening model. The anisotropic broadening is clearly visible in the inset, which shows a pseudo-Voigt fit to the (220)/(022) doublet. The FWHM's were 0.259° and 0.337° for (220) and (022), respectively. The instrumental resolution at this angle is $\sim 0.2°(\Delta Q/Q \sim 2.8\times 10^{-3})$. Mon. cts. refers to the counts recorded in the incident beam monitor.

comparison to $La_{0.5}Ca_{0.5}MnO_3$, the broadening is more diffuse and does not show the pronounced structure previously described in terms of multiple discrete ''phases.'' Furthermore, the strain remains large down to the lowest temperatures, where, as we shall see, it is closely related to the photoinduced phase segregation. In this context, it is important to remark that the peak broadening is also observed in the neutron-diffraction data, and is therefore very unlikely to be a radiation-induced effect. Figure 8 shows a Rietveld refinement pattern of the 2.400 Å neutron data and, in the inset, the individual fit to the (220)/(022) doublet. Both techniques confirm the need to incorporate anisotropic strain and/or particle-size broadening into the peak-shape model in order to correctly fit the data. The presence of local lattice distortions associated with FM clusters, as discussed in Sec. III, could provide an explanation for the observed strain. It is important to point out, however, that the strain is observed well above T_C, indicating that, between T_{CO} and T_C, the cluster spin directions are not correlated.

VI. PHOTOINDUCED PHASE SEGREGATION

Examination of the extended data set obtained at 15 K during the first set of measurements revealed that some of the peaks which are normally single for *Pnma*-type symmetry, such as (220) and (202), were in fact split. Since it was not possible to account for the splitting with a unit cell of lower symmetry, at first sight it appeared that the phase formed initially at 15 K was metastable and transformed partially to a second phase during the 14 h period of data collection. However, the observation at about that time by Kiryukhin *et al.*[45] of an x-ray photoinduced transition below 40 K in a single crystal of $Pr_{0.7}Ca_{0.3}MnO_3$ from an insulating AFM to a metallic FM state made it seem likely that a similar phenomenon was occurring in our powder sample, and that the second phase was in fact the ferromagnetic form. On this basis, the observed splittings can be attributed to a

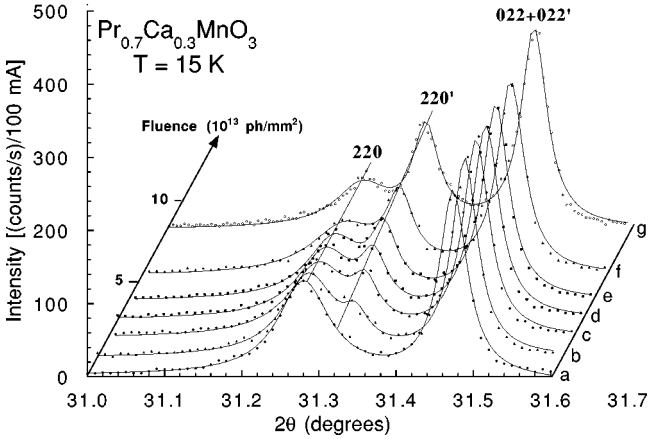

FIG. 9. Synchrotron x-ray diffraction scans of the (220)/(022) doublet at 15 K as a function of x-ray fluence. The elapsed times after the shutter was opened were 5, 132, 274, 393, 504, 677, and 976 min for curves (a)–(g), respectively.

marked contraction ($\sim$0.4%) of the a axis of the ferromagnetic phase (Fig. 5). The evolution of the second phase at 15 K was subsequently followed by scans over narrow angular regions containing the (220)/(022) and (202)/(040) pairs of reflections as a function of time. A few representative scans of the former region at various stages are shown in Fig. 9, as a function of fluence, i.e., the cumulative number of photons/mm^2 incident on the sample as estimated from the count rates recorded by the ion-chamber monitor. Just after cooling to 15 K, there are only two peaks with approximately equal integrated intensities, but (220) is much broader than (022) (FWHM's of 0.079° and 0.046°, respectively), indicative of considerable microstrain along the a-axis direction [Fig. 9, curve (a)]. After $\sim$2 h, there is clear evidence of a shoulder on the high-angle side of the (220) peak [Fig. 9, curve (b)], which becomes a recognizable second peak after $\sim$6 h [Fig. 9, curve (d)], and continues to grow at the expense of the original (220) peak until the end of this set of measurements after $\sim$17 h had elapsed [Fig. 9, curves (e)–(g)]. A least-squares fit to the last data set with three peaks showed some residual discrepancies which were markedly reduced when a fourth peak was added (χ^2 decreased from 2.0 to 1.4), consistent with the presence of a second (022) peak at a slightly lower angle than the original one. The FWHM of the first (220) peak (0.064°) is still relatively large compared to those of the other three ($\sim$0.04°), and changes comparatively little throughout the evolution of the second phase. Because of this and the long tail to the peak which is evident on the low-angle side, the ratio of the integrated intensities of the two (220) peaks obtained from the fit (0.92) is much higher than appears from the relative peak heights in Fig. 9 [curve (g)]. Although it is difficult to extract quantitative values of all the parameters of the two phases from the fits with a four-peak model because of severe correlation problems, especially in the earlier stages, a general picture of the progress of the transformation can be obtained from the fractions of the two phases calculated from the intensities of the respective (220) reflections, which are reasonably well-determined once the second peak is recognizably resolved. The data from the later set of measurements obtained after annealing for 44 h at $\sim$20 K were analyzed in a

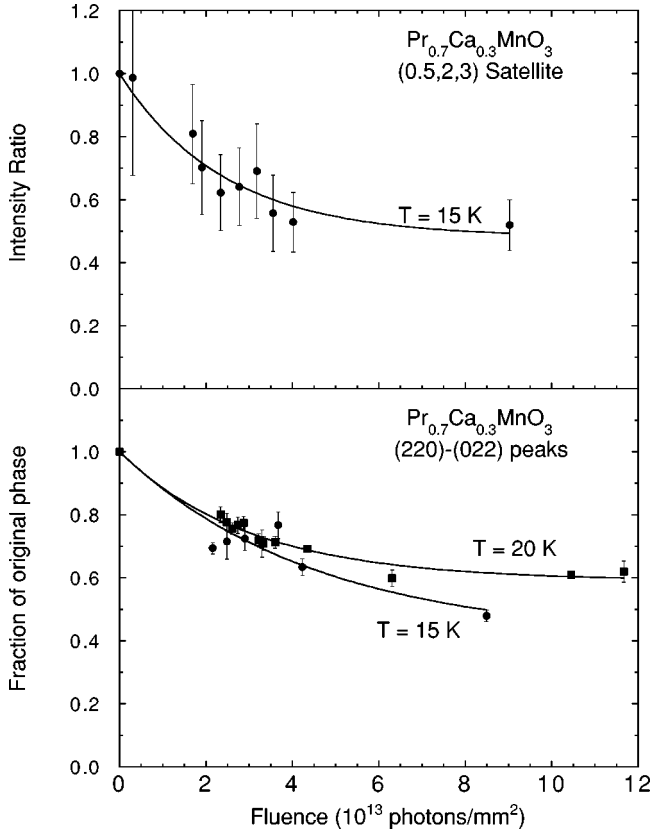

FIG. 10. Photoinduced melting of the CO phase shown as a function of increasing x-ray fluence. (Bottom) Fraction of the original CO phase determined from the ratio of the integrated intensities of (220) and (220)′ at 15 K (squares) and 20 K (circles), (top) intensity ratio I/I(0) for the (1/2 2 3) superlattice reflection at 15 K. Solid lines are guides to the eye.

similar fashion, and the two sets of results are plotted in Fig. 10 (bottom panel) as a function of incident photons. It is noteworthy that no transformation had occurred during the 44 h period of annealing at 20 K when the sample was not exposed to the x-ray beam. The overall trends at 20 K are quite similar to the previous ones, the main difference being that the 20 K data appear to show a saturation effect when about half of the original phase has transformed, which is also apparent from plots of the raw data. It is not clear if this effect is due to the slightly higher temperature, the prolonged annealing period, or some other factor. The lattice parameters of the charge-ordered and the photoinduced ferromagnetic phases at the end of the 20 K run were respectively $a=5.4817(9)$, $b=7.6606(4)$, $c=5.4244(10)$ Å, $V=227.79(6)$ Å^3 and $a=5.4585(2)$, $b=7.6653(3)$, $c=5.4250(3)$ Å, $V=226.99(2)$ Å^3 based on least-squares fits to 9 and 6 reflections, respectively. The a axis and cell volume of the ferromagnetic phase are seen to be significantly reduced by 0.42 and 0.35 %, respectively. Three-point scans of about 20 min duration were also made over the (1/2 2 3) CO peak at selected intervals in an attempt to check if this gradually decreased in proportion to the decrease in the amount of the initial phase. The initial intensity $I(0)$ at 15 K was assumed to be equal to that determined at 80 K from the data shown in Fig. 4. A complete scan of about 2 h duration was made at the end of the run (a portion of this scan is shown in Fig. 3), and the intensity ratio $I/I(0)$ as a

function of incident photons is plotted in Fig. 10 (top panel). Although the error bars are quite large, it is clear that the trend closely parallels that for the (220)/(022) pair in the bottom panel.

The picture of the low-temperature photoinduced effects emerging from the present powder data, in conjunction with the previous single-crystal data presented by Kiryukhin *et al.*,[45] is rather complex, and can be viewed as consisting of two distinct processes occurring simultaneously. The first is a ''phase segregation'' or ''phase organization'' process, which manifests itself in the evolution from a single broad (220) peak into two sharper peaks that can be attributed to the CO and CD phases. There is no unique real-space description of this effect, but a useful model is that of the gradual coalescence of ''droplets'' of the two species into larger homogeneous regions. The second process is the intensity transfer from the (220) to the $(220)'$ peak, which can be described in terms of ''melting'' of the CO phase. The latter effect can be monitored from the intensity of both the superlattice reflections and the main peaks (once they are split), yielding essentially the same dependence as a function of x-ray fluence (Fig. 10). The first process is more difficult to follow quantitatively, as the relevant parameters, i.e., the FWHM's of the (220) and $(220)'$ peaks, are highly correlated in the early stages of phase segregation. However, it can be argued that phase segregation occurs more rapidly than phase melting, since the FWHM's of the two peaks are essentially stable after ~ 6 h of exposure to x rays, at which point only about 50% of the CO phase has transformed to the ferromagnetic CD phase.

VII. SUMMARY

The observation of photoinduced phase segregation as described in Sec. VI constitutes a significant step toward the understanding of the photoinduced insulator-metal transition described by Kiryukhin *et al.*[45] From the present data it is clear that the transition occurs by growth of the metallic phase in the insulating matrix rather than by uniform metallization of a single phase. This mechanism might help to account for the extreme sensitivity of the electrical properties to x-ray exposure, since the conductivity would increase drastically as soon as the percolation threshold is attained for the metallic phase fraction. It is also reasonable to hypothesize that a similar two-phase mechanism might be the basis for both the extremely high values of the magnetoresistance for $Pr_{0.7}Ca_{0.3}MnO_3$ and the strong pressure dependence of the conductivity.

On the basis of the experimental evidence described in the previous sections, the temperature evolution of the structural properties of $Pr_{0.7}Ca_{0.3}MnO_3$ can be summarized as follows.

$T > T_{CO}$. In the CL paramagnetic phase, $Pr_{0.7}Ca_{0.3}MnO_3$ is very similar to other manganates in the same doping range. The large difference between inequivalent Mn-O bond lengths and the large room-temperature Debye-Waller factors indicate the presence of both static and dynamic JT distortions.

$T_N < T < T_{CO}$. In contrast to the ''metallic'' manganates such as $La_{0.7}Ca_{0.3}MnO_3$, $Pr_{0.7}Ca_{0.3}MnO_3$ undergoes a CO transition before the FM transition. The JT polarons freeze into a long-range coherent charge-ordered and orbitally ordered superstructure. The development of lattice strain indicates the presence of inhomogeneities, probably associated with trapped ferromagnetic clusters.

$T_C < T < T_N$. The Mn spins in the CO regions order antiferromagnetically into the pseudo-CE structure.

$T_{irr} < T < T_C$. The spins in the FM clusters become correlated, giving rise to a net ferromagnetic moment on the Mn sublattice.

$T < T_{irr}$. Exposure to x rays induces a complex structural rearrangement which can be described in terms of two distinct processes. First, the broad (220) peak splits into two sharper peaks, consistent with the coalescence of the preexisting clusters into larger regions. Then, the relative intensities of the two peaks and the superlattice peaks change with a longer time constant, consistent with the buildup of the ferromagnetic CD phase at the expense of the antiferromagnetic CO phase.

This complex behavior is quite different from that displayed by other manganese perovskites at the same level of doping, where a single CL-CD transition is observed. We should stress the critical role played in this respect by the electronic bandwidth, controlled through the distortion from cubic symmetry. The unusual properties of $Pr_{0.7}Ca_{0.3}MnO_3$ arise because, due to the narrow bandwidth, the CL-CD transition is suppressed below the freezing point of the JT polarons. However, the richer phase diagram of the narrow-bandwidth manganates stems essentially from the same physics as that of the broad-bandwidth ones. The experimental evidence we have presented can be explained, at least in a qualitative way, by an extended model in which the essential features of the JT and magnetic polaron models are taken into account.

ACKNOWLEDGMENTS

We would like to acknowledge the help of B. Ouladdiaf (ILL, Grenoble) for the D1B data collection and analysis. Work at Brookhaven was supported under Contract No. DE-AC02-76CH00016, Division of Materials Sciences, U.S. Department of Energy. The National Synchrotron Light Source is supported by the U.S. Department of Energy, Division of Materials Sciences and Division of Chemical Sciences.

[1] E. O. Wollan and W. C. Koehler, Phys. Rev. **100**, 545 (1955).

[2] J. B. Goodenough, Phys. Rev. **100**, 564 (1955).

[3] G. H. Jonker and J. H. Van Santen, Physica (Amsterdam) **16**, 337 (1950).

[4] S. Jin, T. H. Tiefel, M. McCormack, R. A. Fastnacht, R. Ramesh, and L. H. Chen, Science **264**, 413 (1994).

[5] A. Urushibara, Y. Moritomo, T. Arima, A. Asamitsu, G. Kido, and Y. Tokura, Phys. Rev. B **51**, 14 103 (1995).

[6] P. Schiffer, A. P. Ramirez, W. Bao, and S-W. Cheong, Phys. Rev. Lett. **75**, 3336 (1995).

[7] H. Y. Hwang, S-W. Cheong, P. G. Radaelli, M. Marezio, and B. Batlogg, Phys. Rev. Lett. **75**, 914 (1995).
[8] Z. Jirák, S. Krupička, Z. Šimša, M. Dlouhá, and S. Vratislav, J. Magn. Magn. Mater. **53**, 153 (1985).
[9] H. Yoshizawa, H. Kawano, Y. Tomioka, and Y. Tokura, Phys. Rev. B **52**, R13 145 (1995).
[10] P. G. Radaelli, D. E. Cox, M. Marezio, and S-W. Cheong, Phys. Rev. B **55**, 3015 (1997).
[11] P. Dai, J. Zhang, H. A. Mook, S.-H. Liou, P. A. Dowben, and E. W. Plummer, Phys. Rev. B **54**, R3694 (1996).
[12] S. J. L. Billinge, R. G. DiFrancesco, G. H. Kwei, J. J. Neumeier, and J. D. Thompson, Phys. Rev. Lett. **77**, 715 (1996).
[13] P. G. Radaelli, M. Marezio, H. Y. Hwang, S-W. Cheong, and B. Batlogg, Phys. Rev. B **54**, 8992 (1996).
[14] J. L. García-Muñoz, M. Suaaidi, J. Fontcuberta, and J. Rodríguez-Carvajal, Phys. Rev. B **55**, 34 (1997).
[15] C. Zener, Phys. Rev. **82**, 403 (1951).
[16] P. W. Anderson and H. Hasegawa, Phys. Rev. **100**, 675 (1955).
[17] P.-G. de Gennes, Phys. Rev. **118**, 141 (1960).
[18] V. Caignaert, E. Suard, A. Maignan, Ch. Simon, and B. Raveau, J. Magn. Magn. Mater. **153**, L260 (1996).
[19] K. Kubo and N. Ohata, J. Phys. Soc. Jpn. **33**, 21 (1972).
[20] K. Kubo, J. Phys. Soc. Jpn. **33**, 929 (1972).
[21] A. J. Millis, P. B. Littlewood, and B. I. Shraiman, Phys. Rev. Lett. **74**, 5144 (1995).
[22] H. Röder, J. Zang, and A. R. Bishop, Phys. Rev. Lett. **76**, 1356 (1996).
[23] A. J. Millis, B. I. Shraiman, and R. Mueller, Phys. Rev. Lett. **77**, 175 (1996).
[24] A. J. Millis, Phys. Rev. B **53**, 8434 (1996).
[25] D. N. Argyriou, J. F. Mitchell, C. D. Potter, D. G. Hinks, J. D. Jorgensen, and S. D. Bader, Phys. Rev. Lett. **76**, 3826 (1995).
[26] C. H. Booth, F. Bridges, G. J. Snyder, and T. H. Geballe, Phys. Rev. B **54**, R15 606 (1996).
[27] T. A. Tyson, J. M. de Leon, S. D. Conradson, A. R. Bishop, J. J. Neumeier, H. Röder, and J. Zang, Phys. Rev. B **53**, 13 985 (1996).
[28] Y. Okimoto, T. Katsufuji, T. Ishikawa, A. Urushibara, T. Arima, and Y. Tokura, Phys. Rev. Lett. **75**, 109 (1995).
[29] S. G. Kaplan, M. Quijada, H. D. Drew, D. B. Tanner, G. C. Xiong, R. Ramesh, C. Kwon, and T. Venkatesan, Phys. Rev. Lett. **77**, 2081 (1996).
[30] K. H. Kim, J. Y. Gu, H. S. Choi, G. W. Park, and T. W. Noh, Phys. Rev. Lett. **77**, 1877 (1996).
[31] R. H. Heffner, L. P. Le, M. F. Hundley, J. J. Neumeier, G. M. Luke, K. Kojima, B. Nachumi, Y. J. Uemura, D. E. MacLaughlin, and S-W. Cheong, Phys. Rev. Lett. **77**, 1869 (1996).
[32] J.-H. Park, C. T. Chen, S-W. Cheong, W. Bao, G. Meigs, V. Chakarian, and Y. U. Idzerda, Phys. Rev. Lett. **76**, 4215 (1996).
[33] A. Shengelaya, G-M. Zhao, H. Keller, and K. A. Müller, Phys. Rev. Lett. **77**, 5296 (1996).
[34] G-M. Zhao, K. Conder, H. Keller, and K. A. Müller, Nature (London) **381**, 676 (1996).
[35] J. W. Lynn, R. W. Erwin, J. A. Borchers, Q. Huang, A. Santoro, J-L. Peng, and Z. Y. Li, Phys. Rev. Lett. **76**, 4046 (1996).
[36] J. M. De Teresa, M. R. Ibarra, P. A. Algarabel, C. Ritter, C. Marquina, J. Blasco, J. Garcí a, A. del Moral, and Z. Arnold, Nature (London) **386**, 256 (1997).
[37] H. Y. Hwang, T. T. M. Palstra, S-W. Cheong, and B. Batlogg, Phys. Rev. B **52**, 15 046 (1995).
[38] A. Maignan, Ch. Simon, V. Caignaert, and B. Raveau, J. Magn. Magn. Mater. **152**, L5 (1996).
[39] E. Pollert, S. Krupička, and E. Kuzmičová, J. Phys. Chem. Solids **43**, 1137 (1982).
[40] Here, and in the remainder of the paper, the standard setting *Pnma* is used to describe the orthorhombic space group for $Pr_{0.7}Ca_{0.3}MnO_3$.
[41] M. R. Lees, J. Barratt, G. Balakrishnan, and D. McK. Paul, Phys. Rev. B **52**, R14 303 (1995).
[42] Y. Tomioka, A. Asamitsu, H. Kuwahara, Y. Moritomo, and Y. Tokura, Phys. Rev. B **53**, R1689 (1996).
[43] J. M. De Teresa, M. R. Ibarra, C. Marquina, P. A. Algarabel, and S. Oseroff, Phys. Rev. B **54**, R12 689 (1996).
[44] H. Yoshizawa, R. Kajimoto, H. Kawano, Y. Tomioka, and Y. Tokura, Phys. Rev. B **55**, 2729 (1997).
[45] V. Kiryukhin, D. Casa, J. P. Hill, B. Keimer, A. Vigliante, Y. Tomioka, and Y. Tokura, Nature (London) **386**, 813 (1997).
[46] P. Thompson, D. E. Cox, and J. B. Hastings, J. Appl. Crystallogr. **20**, 79 (1987).
[47] H. M. Rietveld, J. Appl. Crystallogr. **2**, 65 (1969).
[48] A. C. Larson and R. B. Von Dreele, General Structure Analysis System LAUR 86-748, Los Alamos National Laboratory (1994).
[49] J. Rodríguez-Carvajal, M. Anne, and J. Pannetier, FULLPROF Version 3.2 (Laboratoire Leon Brillouin, Saclay, 1997).
[50] P. G. Radaelli, G. Iannone, M. Marezio, H. Y. Hwang, S-W. Cheong, J. D. Jorgensen, and D. N. Argyriou, Phys. Rev. B **56**, 8265 (1997).